Deposition characteristics of debris flows in a lateral flume considering upstream entrainment

Deposition characteristics of debris flows in a lateral flume considering upstream entrainment

Hongchao Zheng[a], Zhenming Shi[a], Kevin J Hanley[b], Ming Peng[a]*, Shenggong Guan[c]*, Shijin Feng[a], Kunting Chen[d]

[a]Key Laboratory of Geotechnical and Underground Engineering of the Ministry of Education, and Department of Geotechnical Engineering, College of Civil Engineering, Tongji University, China

[b]School of Engineering, Institute for Infrastructure and Environment, The University of Edinburgh, United Kingdom

[c] Key Laboratory of Rock Mechanics and Geohazards of Zhejiang Province, Shaoxing University, China

[d]Institute of Mountain Hazards and Environment, Chinese Academy of Sciences, China

Corresponding author: Ming Peng, pengming@tongji.edu.cn; Shenggong Guan, guanshg@163.com

Abstract The sediment deposited by debris flows in rivers is a common cause of mountain disasters. The deposition characteristics of debris flows are strongly affected by the entrainment during the transportation process and the water depth in the river channel, but how is poorly understood. Here, the effects of the released flow volume, flow density, bed sediment and water depth on the deposition process of debris flows are investigated for a total of 22 different tests. Detailed topographic surveys of deposit lobes are conducted using a 3D laser scanner with high precision. The slopes of lobes are largely determined by the flow density and bed-sediment composition. However, the effect of released flow volume on the lobe slope is relatively limited. The lobe areas projected onto the horizontal plane display dumbbell or trapezoidal shapes depending on deposit volume, and the cross sections along the lateral flume present a Gaussian distribution for flows after bed-sediment entrainment. The lobe area is reduced and lobe height is enhanced with an increase of water depth, contributing to a steeper deposit. Partial, submersed or complete blockages occur, depending on the debris-flow volume and water depth. This study improves understanding of the deposition features and may aid future hazard assessments of debris flows.

Keywords: Debris flows, deposit lobe, entrainment effect, deposition features

1. Introduction

Debris flows generally develop in steep valleys when loose, unconsolidated debris initiates under the action of flow generated by rainfall or snow melting (Pudasaini, 2012; Suwa, 2017). Recent years have seen frequent debris flows due to

earthquakes, severe wildfires, volcanic eruptions, and climate change, resulting in severe casualties and property losses (Jakob and Friele, 2010; Peng and Zhang, 2012; Dowling and Santi, 2014; Stoffel et al., 2014; Shen et al., 2020).

Debris flow injections from gullies into a river generate sediment deposits which can create a significant degree of obstruction of the river section or even a debris dam (Dong et al., 2011; Tang et al., 2011a; Ni et al., 2014; Liu et al., 2014; Shi et al., 2018; Peng et al., 2021; Zheng et al., 2021). The morphology and hydraulic regime of a river are disrupted during the deposition process and a specific type of disruption is the formation of a deposit lobe (Peng and Zhang, 2013; Chen et al., 2019). The deposition characteristics and features of debris flows in a river are far from being understood due to the complexity of the interactions between the incoming solid–liquid mixture conveyed by the debris flow and the receiving river. Such flows have recently been simulated for complex natural events (Shugar et al., 2021) by using the multi-phase mass flow model of Pudasaini and Mergili (2019).

Many research studies have been conducted to investigate geomorphic development of fluvial fans and deltas through laboratory experiments and field surveys (e.g., Bryant et al., 1995; Blair and McPherson, 1998; Bollschweiler et al., 2007; Clarke et al., 2010; de Haas et al., 2016; de Haas et al., 2017). By contrast, several research groups have previously used laboratory flumes to simulate debris flows depositing in a lateral flume (Dang et al., 2009; Liu et al., 2012; Stancanelli et al., 2015; Baselt et al., 2021). The influences of confluence angle, tributary slope, and debris-flow density on the formation process of a deposit lobe have been analyzed.

Three blockage types – complete, partial and submersed blockages can be distinguished from the momentum ratio between flows in the tributary and the mainstream (Dang et al., 2009; Chen et al., 2019). Nevertheless, the effect of the water depth in the lateral flume on the deposit morphology has rarely been investigated (de Haas et al., 2020; de Lange et al., 2020).

Entrainment during the flow process has a significant influence on the deposition characteristics of a debris flow (Pudasaini and Fischer, 2020a). Flow composition can be significantly changed by basal erosion and the pore-fluid pressure and basal shear stresses in the debris flow are thus modified (Coussot et al., 1998; Major and Iverson, 1999; D'Agostino et al., 2010; Hürlimann et al., 2015; Pudasaini and Fischer, 2020a, b). In addition, flow volume is varied: some debris flows grow multifold before deposition while other debris flows have been observed to barely erode (Wang et al., 2003; Godt and Coe, 2007; Berger et al., 2010; Zheng et al., 2018), which further affect the deposit morphology and blockage pattern. The effect of bed-sediment entrainment on the deposit features of debris flow is still poorly understood.

We use a series of experiments to investigate the deposition characteristics of debris flows in a lateral flume. Our main objective is to analyze the effects of debris-flow entrainment and water depth in the lateral flume on the deposit morphology. Secondly, we intend to infer the blockage pattern of debris flows by considering the sediment volume and water depth. Finally, the data obtained from the experiments are important to calibrate and validate true multi-phase mass flow models (e.g., Pudasaini, 2012; Pudasaini and Mergili, 2019).

This paper is structured as follows. First, the experimental flume setup, scaling consideration and debris-flow composition are described. Then, we present observations of the flow behavior during the propagation and deposition stages and analyze the general features of the deposit lobes. Based on these observations, the effects of released flow volume, flow density, bed sediment and water depth on the geometric parameters of the deposit lobes are analyzed. Finally, we briefly show how these experimental results can be applied to natural systems by means of scaling.

2. Methods

2.1 Experimental apparatus

The experimental apparatus consisted of a straight tributary flume 8.0 m long, 0.3 m wide, and 0.4 m deep and a lateral flume 3.5 m long, 0.5 m wide, and 0.5 m deep (Figs. 1 and 2). The tributary flume was aligned with the middle of the lateral flume with an angle of 90°. The tributary flume was fixed at an angle of 18° to the horizontal plane and the lateral flume was horizontal for all of the experiments. The bottoms of both flumes were riffled steel plates roughened by small bulges with a roughness height of 1.6 mm to simulate natural channel roughness. Three overflow gates at heights h of 0 cm, 8 cm and 16 cm were installed at both ends of the lateral flume in order to control the water depth in the lateral flume (Fig. 2).

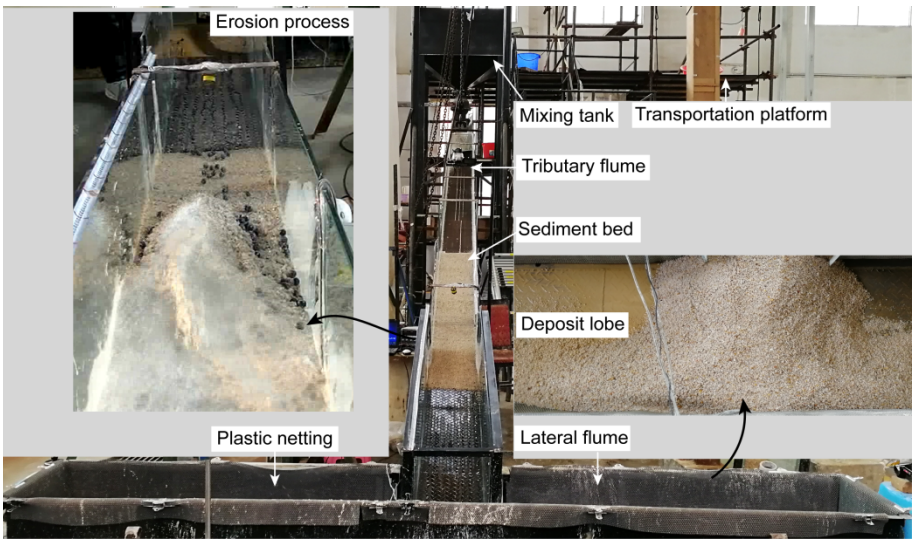

Fig. 1. Experimental apparatus for debris-flow entrainment and deposition. The inset on the left shows the flow front encountering coarse-grained bed sediment; the inset on the right shows a deposit lobe in the lateral flume.

Various instruments have been used for investigating the propagation and deposition of debris flow (Fig. 2). Three video cameras (GZ-R10BAC, JVC, 1920 x 1080 pixel) were employed to record the transportation process of debris flows from the top of the tributary flume. Another camera was used to record the deposition process from one side. A high-speed camera (i-SPEED7, iX Cameras) installed perpendicular to the direction of the tributary flume was used to observe the entrainment process. A 3D laser scanner (ScanStation P40, Leica, measurement accuracy 1.2 mm+10 ppm) was employed to obtain the morphology of each deposit lobe in the lateral flume.

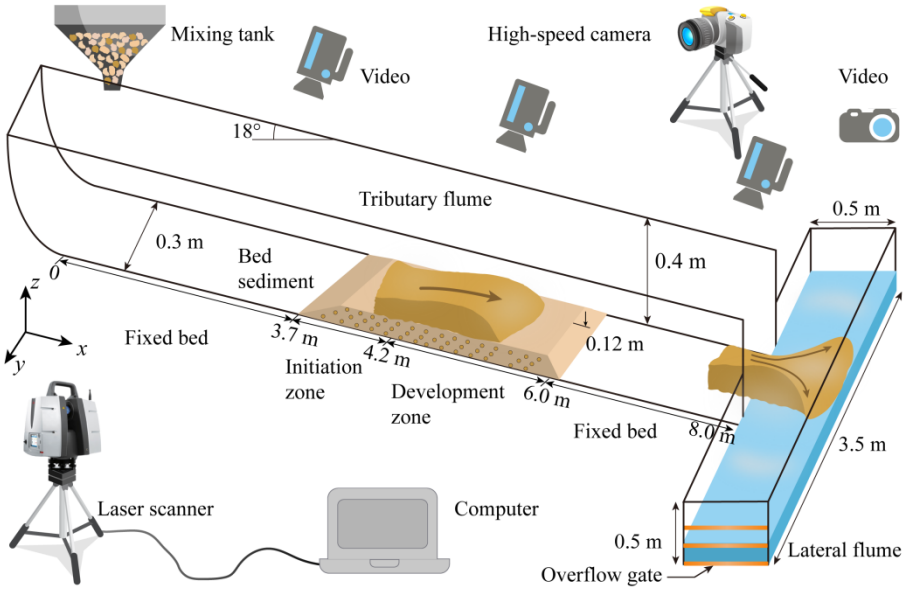

Fig. 2. Sketch of the complete experimental apparatus.

2.2 Scaling consideration

The methodology for scaling findings from the laboratory tests to prototype conditions assumes geometric, kinematic and dynamic similarity. Geometric similarity is given by the ratio of the prototype depth h^* and laboratory depth h conditions,

$$\lambda = \frac{h^*}{h} = 80 \tag{1}$$

The Froude scaling concept is applied in our experimental tests (Domnik and Pudasaini, 2012; de Lange et al., 2020):

$$\frac{v^*}{\sqrt{gh^*\cos(\theta)}} = F_r = \frac{v}{\sqrt{gh\cos(\theta)}} \tag{2}$$

Here, v^* and v are the prototype and laboratory flow velocities, respectively. g is the gravitational acceleration. θ is the slope of the channel.

The selected laboratory and prototype parameters for this study, satisfying Froude scaling and based on the characteristic length scale, are compared (Table 1).

The width of a trunk stream is usually more than twice that of a debris flow gully at the confluence, as for the Hongchun gully (Tang et al., 2011a), Sanyanyu gully (Tang et al., 2011b) and Kamimaihorizawa gully (Suwa, 2017). Tributary streams have a smaller width. For example, the widths of Hougou gully and Majingzi gully (22–44 m) are less than twice that of Nanya River (30–55 m), which is a tributary of Dadu River (Ni et al., 2014). The width of Xiongjia gully (36–45 m) is nearly equal to that of Zhuma River, which is a tributary of Nanya River. Considering that a tributary stream is susceptible to blockage by a debris flow, the ratio of lateral flume to tributary flume widths in our experiments is chosen as 1.67. Froude numbers of the debris flows F_{rd} measured in our experiments were 0.4–5.2. Froude numbers of water F_{rm} in the lateral flume are smaller than 1.0, considering the gravity of the flow prevails over the inertia for the static water (de Haas et al., 2020; de Lange et al., 2020). The flow velocity is thus smaller than 7.9 m/s for the prototype flow with a water depth of 6.4 m. The longitudinal gradient of the riverbed is smaller than 0.013 when the Manning coefficient n = 0.05. This longitudinal gradient matched the slopes of Nanya River (0.008–0.014) close to Majingzi gully and Zhuma River (0.01–0.02) close to Xiongjia gully (Ni et al., 2014).

Table 1. Range of laboratory and prototype parameters for the experiments

Parameters	B_t (m)	B_m (m)	v (m/s)	h_d (m)	h (m)	F_{rd}	F_{rm}
Laboratory	0.3	0.5	0.4–2.2	0.02–0.08	0, 0.08, 0.16	0.4–5.2	<1.0
Prototype	24	40	3.6–19.6	1.6–6.4	0, 6.4, 12.8	0.4–5.2	<1.0

Note: B_t and B_m denote the widths of the tributary flume and lateral flume,

respectively. h_d is the flow depth of a debris flow entering into the lateral flume.

2.3 Experiments and procedure

The experimental procedure was that the debris flows were firstly triggered by entraining the sediment beds in a tributary flume which then flowed into a lateral flume. The debris flows were eventually deposited under the reworking action of a preset water depth. The relevant parameters varied in the experiments were the released density ρ_i, flow volume V_0, bed type, and water depth h in the lateral flume (Table 2).

To simulate the processes of initiation and development of a natural debris flow, the experimental debris flows presented here were triggered by released flows eroding the sediment beds (widely graded and coarse-grained). The initiation zone was determined to be located from x = 3.7–4.2 m (Fig. 2), considering that the flow-front velocity remained stable after this zone and a steady flow nose can be developed after the entrainment of the coarse-grained bed sediment in this zone. The development zone was located from x = 4.2–6.0 m. The entrainment volume discussed in the following sections referred to entrainment of bed sediment in the development zone (Pudasaini, 2012; Mergili et al., 2017; Kafle et al., 2019).

The released bulk densities ρ_i from the mixing tank were 1000 kg/m^3 (water), 1500 kg/m^3 or 1700 kg/m^3 for producing debris flows with different densities. After the released flows of bulk density 1000 kg/m^3 migrated over the initiation zone, the flow-front densities of the debris flows increased to 1470–1560 kg/m^3. For the released bulk flows of density 1500 and 1700 kg/m^3, the flow-front densities of the

debris flows were 1590–1730 and 1790–1870 kg/m^3, respectively, downstream from the initiation zone. The material composition of the developed flows suggest that these are complex and truly multi-phase flows (Pudasaini and Mergili, 2019; Mergili et al., 2020).

The volumes of these released flows V_0 were 0.04 m^3 or 0.07 m^3. The water and debris sediment were adequately mixed using a portable rotary mixer before releasing the flow. The sediment beds averaged 12 cm in thickness and covered the bottom surface of the tributary flume (Fig. 1). The dry densities of bed sediments were 1500±50 kg/m^3 and porosities were 0.44±0.02 in all experiments. The bed sediment was moistened by spraying water until considerable water was seeping out. The mass water content w was 0.11±0.02 for the widely graded bed sediments and 0.06±0.02 for the coarse-grained bed sediments due to the difference in their water retention capacities. Four released flows passing through the fixed bed in tests 1–4 were designed to compare the deposition characteristics of flows after the entrainment of bed sediment.

According to video recordings, the maximum flow depth entering the lateral flume was approximately 8 cm. The water depths h in the lateral flume were set at 0 cm, 8 cm or 16 cm by three overflow gates (Fig. 2), allowing for the water depth to be lower than, equal to or higher than the flow depth. The overflow gate at the preset height was kept open during the processes of debris-flow runout and deposition. When debris flow rushed into the lateral flume, water overflowed from the corresponding overflow gate. The water depth at the end of the lateral flume was kept

approximately constant during the whole process in order to minimize the boundary effect parallel to the lateral flume. After the deposition process had finished, the slurry in the lateral flume was released via the bottom overflow gate. The complete deposit morphology of each lobe was captured by the 3D laser scanner.

Table 2 Parameters for the different tests

Experiment	V_0 (m^3)	ρ_i (kg/m^3)	Bed	h (cm)
1	0.04	1500	F	0
2	0.07	1500	F	0
3	0.04	1700	F	0
4	0.07	1700	F	0
5	0.04	1000	W	0
6	0.07	1000	W	0
7	0.07	1000	W	8
8	0.04	1000	C	0
9	0.07	1000	C	0
10	0.07	1000	C	8
11	0.07	1000	C	16
12	0.04	1500	W	0
13	0.07	1500	W	0
14	0.07	1500	W	8
15	0.04	1500	C	0
16	0.07	1500	C	0
17	0.07	1500	C	8
18	0.04	1700	W	0
19	0.07	1700	W	0
20	0.04	1700	C	0

21	0.04	1700	C	8
22	0.07	1700	C	0

Note: F = fixed bed, W = widely graded sediment bed, C = coarse-grained sediment bed.

2.4 Composition of released flow and bed sediment

The grain composition of the released flows referred to Hsiaolin debris flow, as shown in Fig. 3 (Dong et al., 2011). Based on released flow material, the grading curves of widely graded and coarse-grained bed sediments were derived. The size distribution of the widely graded bed sediment matched that of the released debris flow, excluding the fine component (0.001–0.01 mm). The overall debris composition can be considered to remain the same during the entrainment process. Coarse-grained bed sediment consisted of coarse sand (1–2 mm) and gravel (2–5 mm). The coarse fraction of debris flow increased when the released flow migrated over the coarse-grained bed sediment (de Haas and van Woerkom, 2016; Pudasaini and Fischer 2020b).

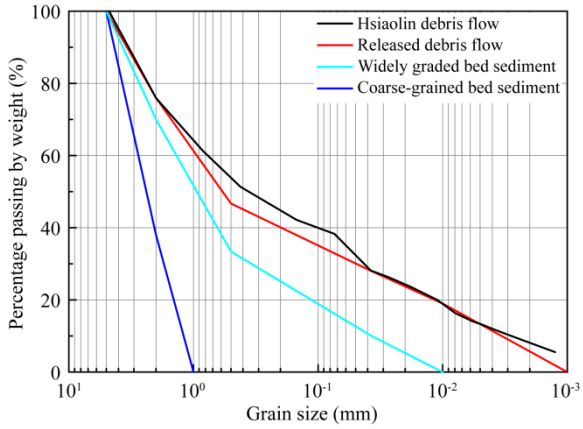

Fig. 3. Grain compositions of the Hsiaolin debris flow in Taiwan (Dong et al., 2011), released flow, widely graded and coarse-grained bed sediments.

From constant-head permeameter tests, the saturated permeability coefficients k

of the widely graded and coarse-grained bed sediments at the same dry density in the entrainment process were measured (Table 3). Considering the large displacement and deformation of bed sediment in the processes of erosion and deposition, we conducted ring shear tests (GCTS, SRS-150) to obtain the shear strengths (cohesion c and internal friction angle φ), as shown in Fig. S1. The internal friction angle φ of the widely graded bed sediment was smaller than that of the coarse-grained bed sediment.

Table 3. Geotechnical properties of bed sediment

Sediment type	Grain composition	d_{50} (mm)	k (cm/s)	c (Pa)	φ (°)
Widely graded	Silt, sand, gravel	0.9	0.07	0	27.2
Coarse-grained	Coarse sand, gravel	2.4	2.76	0	33.3

2.5 Data collection and processing

Two samples were collected just after flows migrated over the initiation zone and entered the lateral flume. These samples were dried in an oven to calculate the bulk density at the flow front. Three samples of bed sediment were collected and dried in the oven to calculate the mass water content. The flow-front velocity of debris flow during its runout to the lateral flume was calculated from three video cameras and the scaleplate on the surface of the tributary flume sidewall (Fig. 2). The flow depth was measured using the high-speed camera and the scaleplate pasted on the flume sidewall.

The data processing of point clouds from the 3D scanner was conducted as follows. As shown in Fig. 4, point clouds of the deposit lobe were firstly extracted from the whole experiment site. These point clouds were then incorporated together

from three scans in different locations, in order to avoid the obstruction created by the sidewalls of the tributary flume and lateral flume. The spatial distributions of each deposit lobe were determined by subtracting the elevations of the lobe and bottom of the lateral flume. Finally, point clouds were displayed with MATLAB (The MathWorks, version R2018a) using natural neighbor interpolation to obtain a gridded DEM (Digital Elevation Model) of 3 mm resolution. The point clouds of bed sediment in the tributary flume were processed as for each deposit lobe. The entrainment volume was calculated by adding all the volumes of net bed erosion (de Haas and van Woerkom, 2016; Pudasaini and Fischer, 2020a).

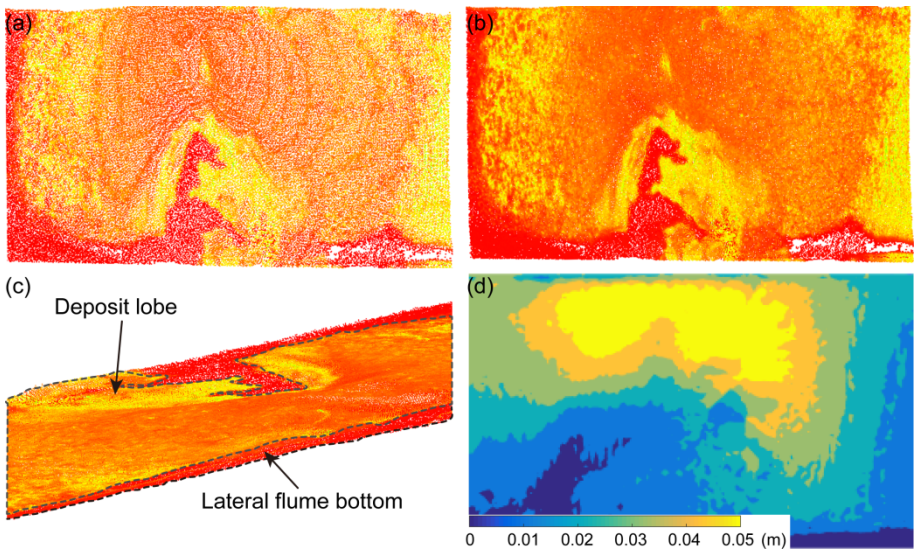

Fig. 4. Data processing of point clouds: (a) extraction of a point cloud for a deposit lobe from a scan; (b) incorporation of point clouds of three scans denoted as the increase in point density; (c) point clouds of a deposit lobe and bottom of the lateral flume obtained by adjusting the spatial coordinate system; (d) gridded DEM of a deposit lobe using natural neighbor interpolation. Figs. (a), (b) and (d) are the top views of a deposit lobe and Fig. (c) is the side view of a deposit lobe and bottom of the lateral flume.

The DEM of a deposit lobe was used for visualization and to measure the geometric parameters such as lobe width, height, length, and area (Fig. 5). The lobe width was characterized as the maximum deposit width perpendicular to the lateral flume. The lobe height was the maximum deposit thickness. The lobe length was defined as the maximum deposition length parallel to the lateral flume. The lobe area was the area of the deposit projected on the horizontal plane. The slope angle of the lobe was calculated as the lobe height divided by half of the lobe length. In addition, the longitudinal and transverse sections of a deposit lobe at any location and the shape of a lobe area were also extracted from the DEM.

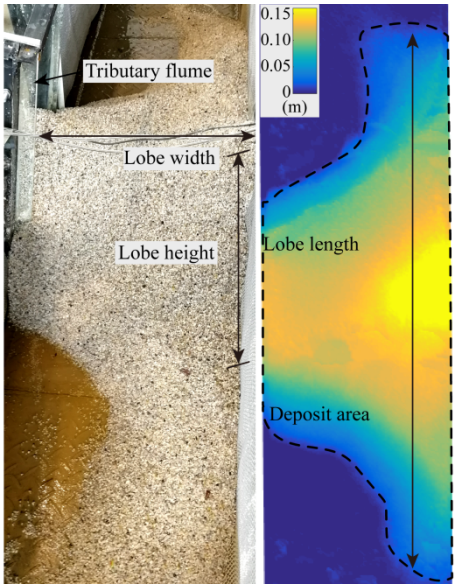

Fig. 5. Geometric parameters of debris flow deposits: lobe width, height, length and area in the dotted box: (a) experimental picture of a debris flow deposit (test 10); (b) the corresponding DEM of the deposit lobe.

3. Debris flow motion in the tributary flume and the lateral flume

3.1 Propagation stage of debris flow

Regardless of released density or volume, the flow-front velocity on the fixed

bed (tests 1–4) was approximately 2.0 m/s when debris flow entered the lateral flume (Table S1). The flow-front velocity of flows after the entrainment of widely graded bed sediment (FEW) ranged from 1.3–1.6 m/s. It was 0.5–0.8 m/s for flows after the entrainment of coarse-grained bed sediment (FEC) due to the differences of internal friction of the flow front and boundary friction of bed sediment. Flow in test 8, which had a slow flow-front velocity of 0.4 m/s, was an exception.

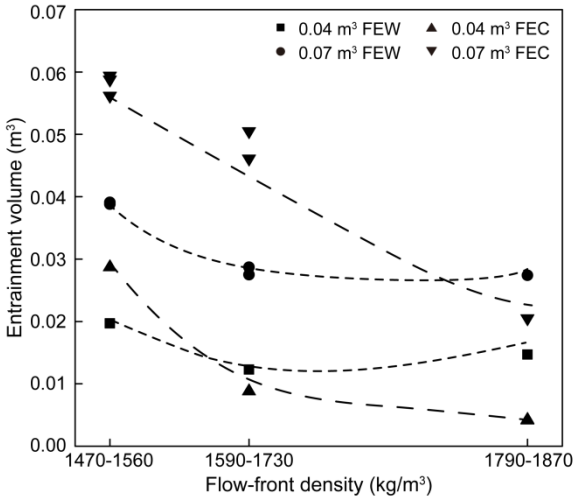

Fig. 6. Entrainment volume of the sediment bed for a total of 18 tests. The difference of entrainment volumes is very small between experiments under the same conditions and data points often overlap.

As shown in Fig. 6, the entrainment volume of bed sediment had a large variation ranging from 0.004–0.0588 m^3. Regardless of flow-front density, the entrainment volume of bed sediment increased with the released flow volume. The reason was that 0.07 m^3 released flow had a higher flow depth than 0.04 m^3 released flow (Table S1), resulting in a higher erosion rate (Pudasaini and Fischer, 2020a). Under the same released volume, the entrainment volume of debris flow decreased with the increase of flow-front density on the coarse-grained bed sediments. The

entrainment volume decreased first and then increased with flow-front density on the widely graded bed sediments. The entrainment volumes of widely graded bed sediment were generally smaller than those of coarse-grained bed sediment for debris flows with flow-front densities of 1470–1560 and 1590–1730 kg/m^3. However, the converse was observed for debris flows with flow-front densities of 1790–1870 kg/m^3 because part of the debris flows was deposited on the coarse-grained sediment bed for tests 20–22.

3.2 Deposition stage of debris flow

The flow front of debris flow was continuously shouldered aside into lateral levees when entering the lateral flume with a water depth h = 0 (Fig. S2). These levees laterally confined the subsequent flow to migrate towards the opposite sidewall of the lateral flume. The lateral levees were also observed for subaerial and subaqueous debris flows conducted by de Haas et al. (2020). Then, the lateral levees were covered by the returned flow and restarted to migrate parallel to the lateral flume. The subsequent flow entering the lateral flume was strongly mixed with the returned flow rebounding from the opposite sidewall.

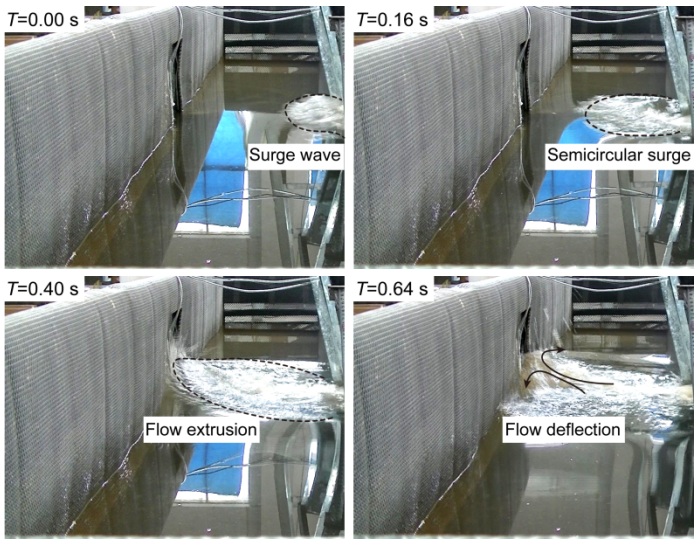

Fig. 7. Deposition process of debris flow in the lateral flume in test 10. Debris flow was just entering the lateral flume at T=0.00 s.

When debris flow rushed into the lateral flume with a water depth h = 8 or 16 cm, a semicircular surge wave developed at the exit of the tributary flume which then moved towards the opposite sidewall of the lateral flume (Fig. 7). The water near the opposite sidewall of the lateral flume was extruded. Due to the strong debris impact to the water body and the associated momentum exchange (Kafle et al., 2019), the water depth dramatically increased in the middle of the lateral flume and near the opposite sidewall of the lateral flume, compensated by a reduction in water depth close to the tributary exit. This phenomenon was termed a hydrodynamic impact vacuum by Pudasaini (2014). Part of the flow deflected to move parallel to the lateral flume and part of the flow even reversed on itself due to the obstruction of the opposite sidewall. The maximum flow height at the opposite sidewall of the lateral flume reached up to 25 cm for flows with various released volumes: significantly larger than the water depth in the lateral flume. The water in the lateral flume was strongly rolled and stirred, indicating that debris flow was intensively mixed. The water moved to the

opposite sidewall of the lateral flume at the deposit zone and it was reversed away from the deposit zone.

As shown in Fig. 8, a bedding structure of coarse gravel was developed at the surface of the lobes. The debris flow entering the lateral flume was strongly mixed with the surges rebounding from the opposite sidewall or water in the lateral flume (Figs. S2 and 7). The debris sediment was poorly sorted during the deposition process and significant grain sorting such as grading or an inverse grading sequence was not observed below the bedding structure. The finer grains on the surface of the lobe were carried away by the subsequent dilute flow and deposited far from the deposit lobe, while the coarser grains were left behind. The stratigraphic characteristics of the experimental debris flow presented here was consistent with the observations from large-scale deposit experiments at the U.S. Geological Survey that particles coarser than about 8 mm were concentrated at or near the surface of debris-flow deposits (Major, 1995).

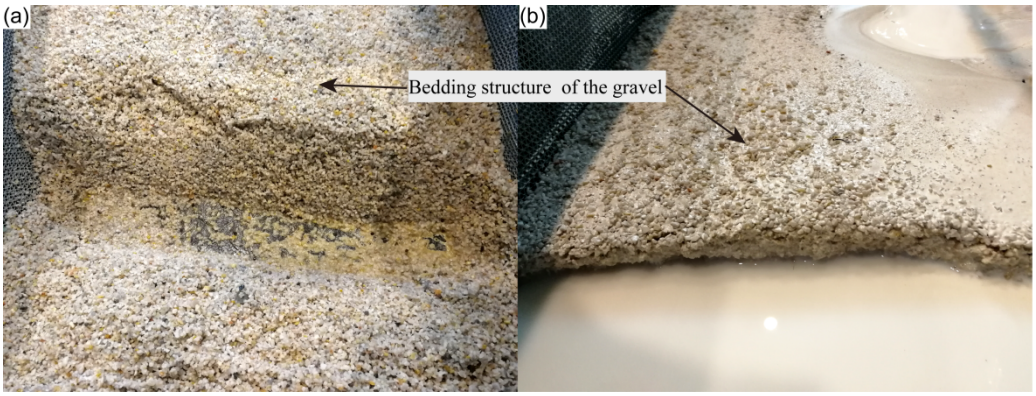

Fig. 8. Grain distributions of selected experimental debris flows: (a) test 9 and (b) test 13.

4. Morphology of debris-flow lobes

4.1 Deposit shape

The shapes of deposit lobes displayed significant differences, affected by the entrained sediment (Figs. 9 and 10). The depositions of flows without sediment entrainment took the form of a typical alluvial fan compressed by the opposite sidewall of the lateral flume. Due to a high flow velocity (2 m/s), the deposited debris concentrated at the opposite sidewall of the lateral flume and slurry containing the fine component was deposited at the tributary exit (Figs. 9a and 9b). This phase separation between the coarse and slurry material was modelled by the mechanical phase separation model by Pudasaini and Fischer (2020b). The lateral flume was partially blocked. The lobe height ranged from 0.04–0.06 m and lobe length was 0.98–1.45 m in tests 1–4. The lateral flume was completely blocked by the FEW and thus the lobe width was the same as the flume width. The lobe height ranged from 0.07–0.14 m and lobe length was 0.84–2.24 m. Compared with the FEW, the depositions had the shape of a swollen lobe for the FEC inferred from Fig. 10.

Fig. 9. Deposition morphology of selected experimental debris flows. (a, b) The depositions of flows without entrainment in tests 1 and 2 take the form of typical alluvial fan compressed by the opposite sidewall of the lateral flume. Slurry containing fine components is deposited in the dashed box. (c, d) Deposit lobes of FEC in tests 9 and 10. (e, f) Deposit lobes of FEW in tests 12 and 13. (g, h) Deposit lobes of FEC in tests 15 and 16. The tributary exit is on the right of each picture and the opposite sidewall of the lateral flume is on the left.

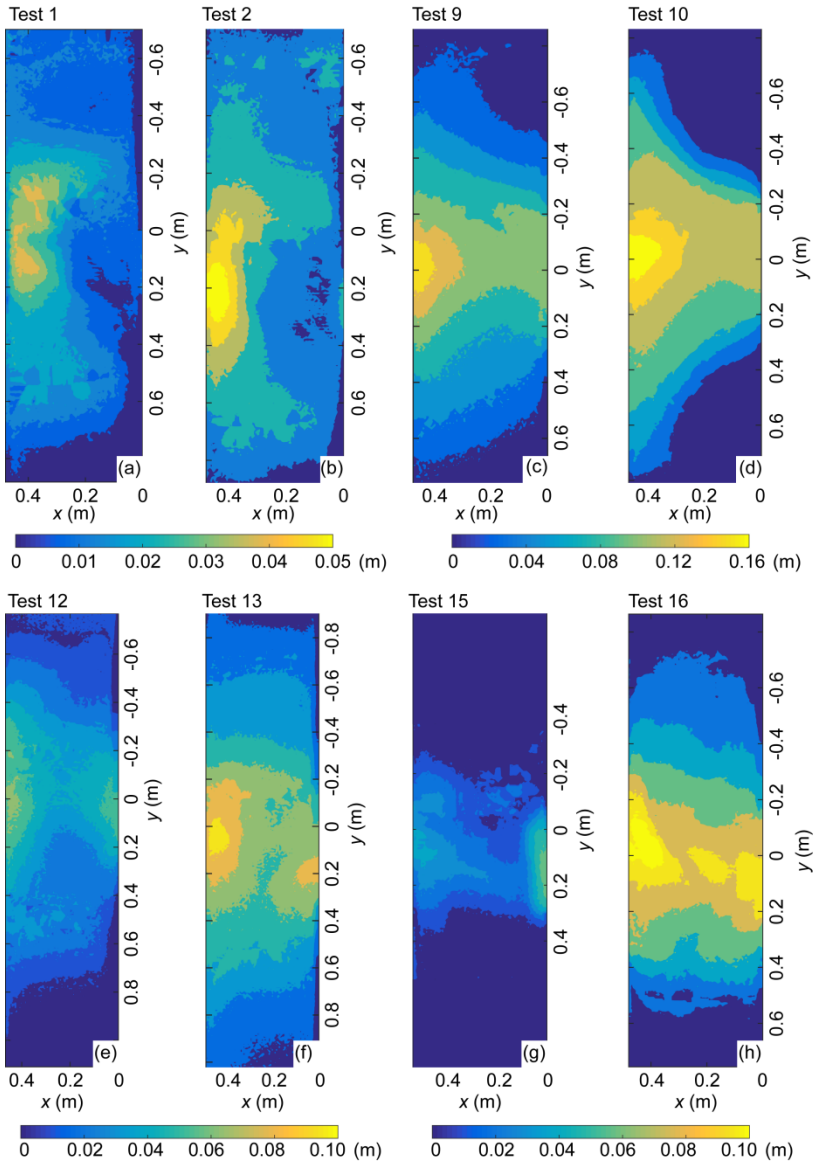

Fig. 10. The DEM of deposition lobes in selected experimental debris flows: (a-b) tests 1 and 2, (c-d) tests 9 and 10, (e-f) tests 12 and 13, (g-h) tests 15 and 16. *x* increases from the tributary flume exit to the opposite sidewall of the lateral flume.

The deposit areas of flows after sediment entrainment projected onto a horizontal plane were shaped as dumbbells or trapezoids for 0.04 m^3 and 0.07 m^3 released flows, respectively, except for tests 8 and 18 (Figs. 11 and 12). Debris flow gradually deposited from the opposite sidewall of the lateral flume to the tributary flume exit. The initial flows with a higher flow velocity were deposited near the opposite

sidewall of the lateral flume due to limited debris sediment for 0.04 m^3 released flows and the subsequent flows with a low flow velocity were deposited at the tributary exit. The lobe lengths at both sidewalls of the lateral flume were larger than the length in the middle of the lateral flume. The shape of the deposition area thus resembled a dumbbell (Figs. 11a and 11b). By contrast, the lateral flume is completely blocked by the initial flows for 0.07 m^3 released flows and the subsequent flows covered the surface of the deposition accumulated from the initial flows. The deposit sediment near the opposite sidewall of the lateral flume was pushed by the subsequent flows and moved parallel to the lateral flume. The deposit length near the opposite sidewall of the lateral flume was larger than that at the tributary exit. The shape of the deposition area thus resembled a trapezoid (Figs. 11c and 11d).

Tests 8 and 18 were an exception. An alluvial fan was formed close to the exit of the tributary flume in test 8 due to a low flow velocity (0.4 m/s). For test 18, the released density was high (1700 kg/m^3) and the entrainment volume was relatively large (0.015 m^3). The debris sediment in the initial flow was sufficient to block the lateral flume, which was similar to the deposition process of 0.07 m^3 released flow.

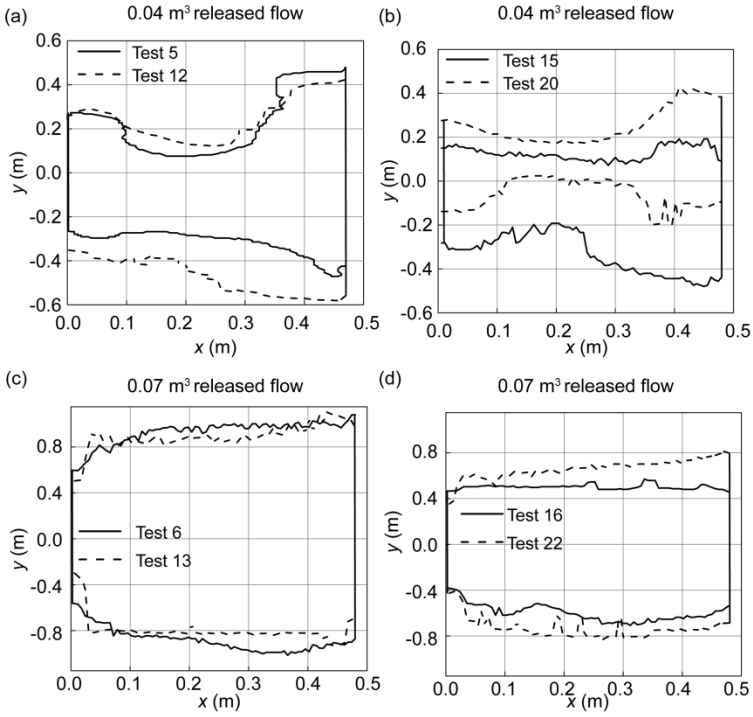

Fig. 11. Deposition area of flows after sediment entrainment: (a) (b) dumbbell-shaped (tests 5, 12, 15 and 20) and (c) (d) trapezoidal (tests 6, 13, 16 and 22).

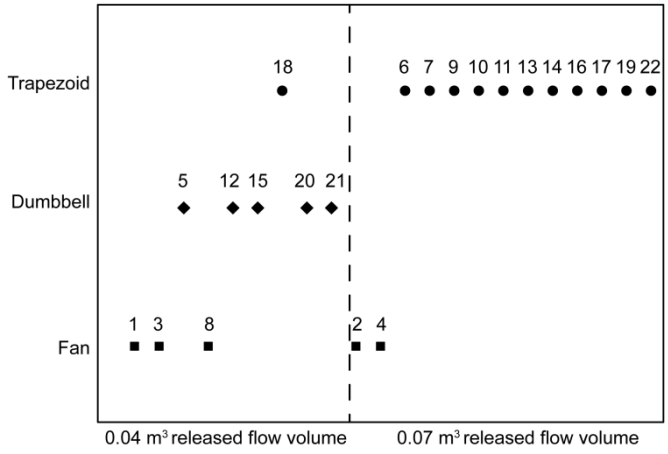

Fig. 12. Effect of released flow volume on the horizontal shape of the deposits. The number denotes the individual test.

4.2 Longitudinal section

The longitudinal section of each lobe along the lateral flume was extracted from the scanned DEM. As shown in Fig. 13, longitudinal sections at each location

presented a Gaussian distribution for flows after the entrainment of widely graded and coarse-grained bed sediments,

$$z = Ae^{\frac{-(y-y_c)^2}{2w^2}} \tag{3}$$

where A is the lobe height, y_c is the mean value, and w^2 is the variance. The longitudinal sections of lobes were not completely symmetrical about the tributary flume due to flow disturbance at the entrance to the lateral flume, and probably due to other fluid dynamical effects.

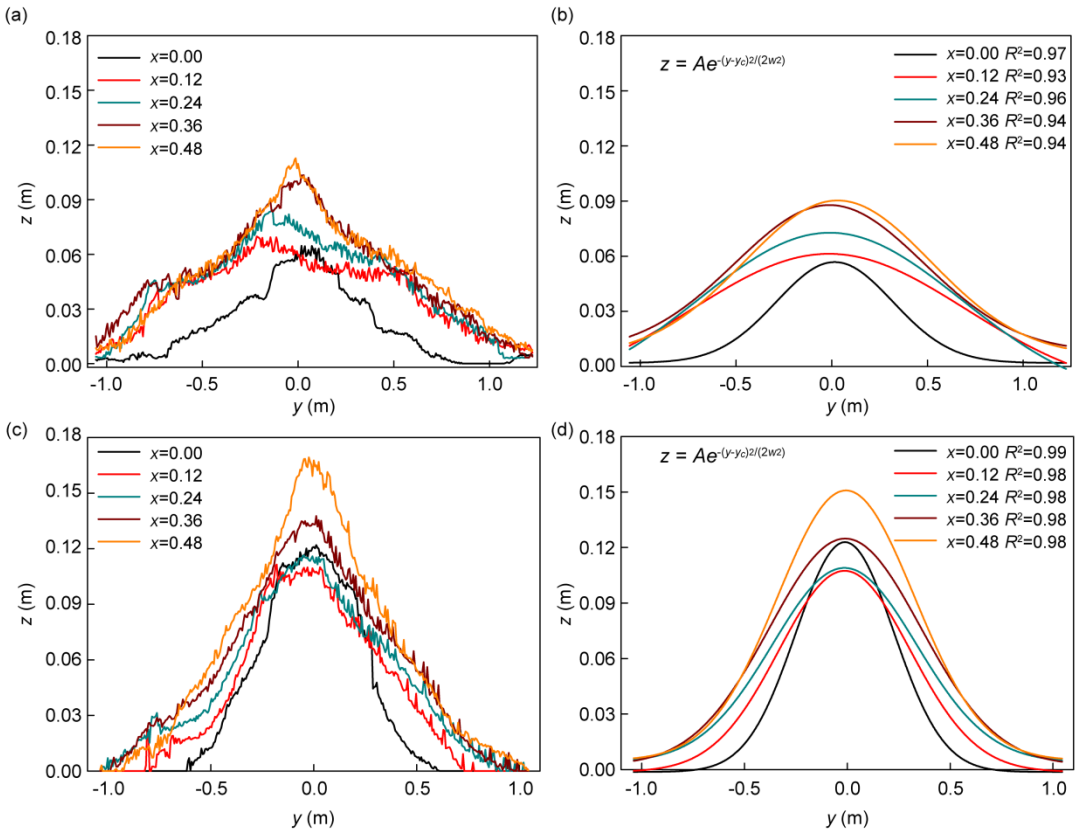

Fig. 13. Longitudinal sections of the lobes: experimental values obtained by the DEM of deposition lobes and values fitted by a Gaussian function in (a) and (b) test 6; (c) and (d) test 9. R^2 is the coefficient of determination.

The longitudinal sections of lobes varied in the direction perpendicular to the lateral flume (Fig. 13). The deposition heights at the opposite sidewall of the lateral

flume were larger than those at the tributary flume exit. This was consistent with the observation of debris-flow lobes at Hsiaolin village (Dong et al., 2011) and Xiongjia gully (Ni et al., 2014). For released flow with the same density, the variance w^2 of cross sections was larger for the FEW than for the FEC in the same location, indicating that the cross sections of the FEW were tabular but swollen for the FEC.

4.3 Transverse section

The transverse section perpendicular to the lateral flume is shown in Fig. 14. The deposition height gradually increased from the tributary flume exit to the opposite sidewall of the lateral flume for deposit sediment out of the tributary flume. The sediment was deposited by the initial flows due to the obstruction of the opposite sidewall of the lateral flume (Fig. S2). This is consistent with the observation of debris flow in Xiongjia gully that flows rushed across Zhuma River with velocity 12–14 m/s before stopping at the opposite side (Ni et al., 2014). The deposit sediment at the opposite sidewall of the lateral flume had a larger height than that at the tributary flume exit. However, the deposition height decreased first and then increased from tributary flume exit to the opposite sidewall of the lateral flume for deposit sediment within the tributary flume. The subsequent flows with a low velocity were deposited at the tributary flume exit and thus had a larger deposition height than that in the middle.

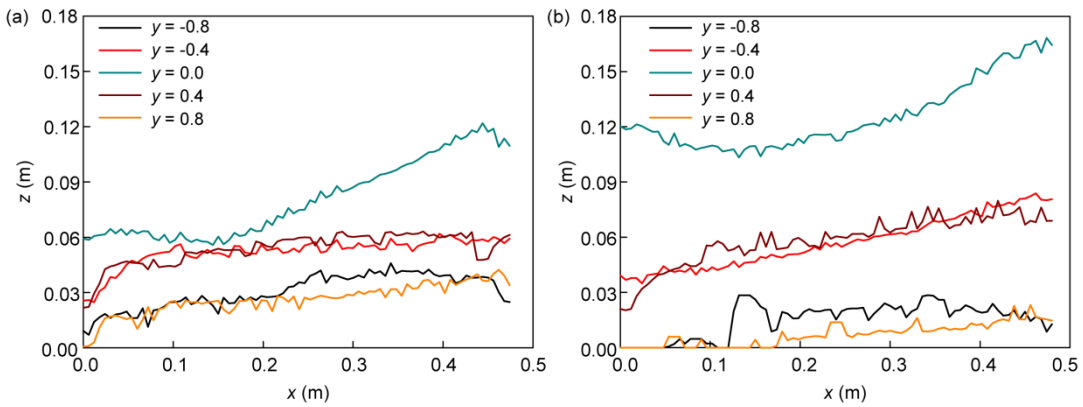

Fig. 14. Transverse section of the lobes in (a) test 6 and test 9.

5. Geometrical parameters of deposit lobes

5.1 Effects of entrainment and released flow on deposit lobes

As shown in Fig. 15, the lobe heights of flows after entrainment of the sediment bed were larger than those of flows on the fixed bed with the same released volume due to the increase of sediment volume. The lobe height increased with the increase of the entrainment volume of the sediment bed. The trend of lobe height with the flow-front density was consistent with that of the entrainment volume of bed sediment with the flow-front density by comparing Figs. 6 and 15.

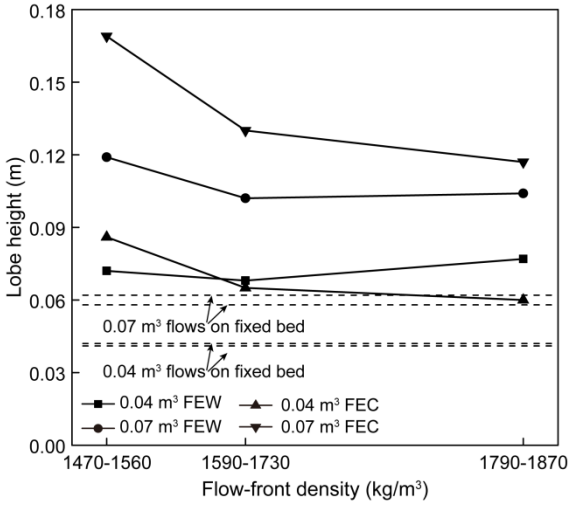

Fig. 15. Effects of flow volume and flow-front density on the lobe height.

The lobe slope angle of the experimental debris flows varied from 5–15° (Fig.

16). This is suitable for the debris flows triggered by the Morakot typhoon which had a slope angle of 4–20° (Chen et al., 2019) and the debris flows in Yinxiu which had a slope angle of 5–22° (Tang et al., 2011a).

The ratios of lobe height to lobe length of flows without the entrainment of bed sediment were approximately 0.04: smaller than the ratios for flows after erosion on the sediment bed (Fig. 16). The reason is that the flow density increased after bed entrainment and the shear resistance of debris sediment during the deposition process was accordingly enhanced. The velocities of flows on the fixed bed were higher than those of flows on the sediment bed (Table S1). The ratio of lobe height to lobe length of the FEC ranged from 0.07–0.13 which was higher than the value of the FEW. The reason is that the proportion of coarse sand and gravel in the debris flow increased after entrainment of coarse-grained bed sediment. The basal shear stress of debris flow was enhanced and the flow velocity was relatively small (0.87–1.04 m/s). In addition, the shear strength of debris sediment during deposition was high, contributing to a swollen deposit. By contrast, the debris composition overall remained the same during the entrainment of widely graded bed sediment. The velocity of debris flow was higher (1.41–1.59 m/s) and the shear strength was relatively small. A simplified calculation was conducted to estimate the ratio a of the basal shear stress R_s of the FEW and FEC,

$$a = \frac{R_{sw}}{R_{sc}} \tag{4}$$

$$R_s = c + \left(\rho - \rho_f\right)\cos\theta g H \tan\varphi \tag{5}$$

where ρ and ρ_f were flow-front density and slurry density, respectively. c is the

cohesion of bed sediment (Table 3). *H* was flow depth (Table S1). *a* values were 0.24 and 0.23, respectively, by comparing tests 5 and 8 and tests 6 and 9, indicating that the basal shear stress of FEW was significantly smaller than that of FEC.

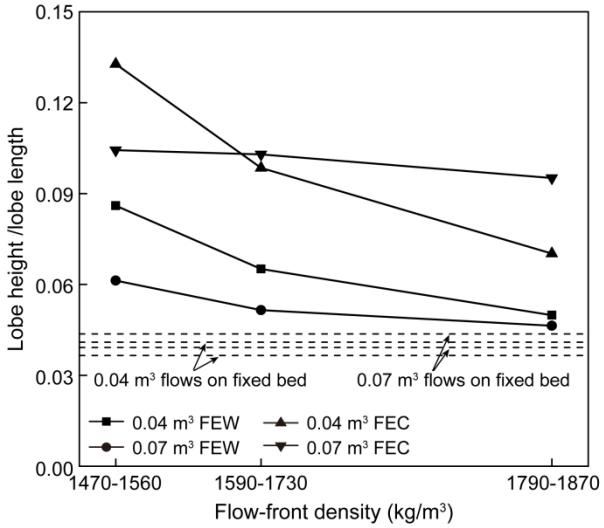

Fig. 16. Effects of flow volume and flow-front density on the ratio of lobe height to lobe length.

The ratio of lobe height to lobe length decreased with flow-front density for all of the tests (Fig. 16). Slurry density increased with the increase of released density for the experimental debris flows presented here (Table S1). The viscosity of slurry increased due to small amounts of clay (Major and Pierson, 1992). Seeps and small springs developed on lobe surfaces formed by flows with flow-front densities 1790–1870 kg/m^3 (Fig. S3). No water escaped the lobes formed by flows with flow-front densities 1470–1560 kg/m^3. The excess pore pressure dissipated after deposition by flows with high densities due to a low hydraulic diffusivity (de Haas and van Woerkom, 2016). Affected by the excess pore pressure, the basal shear stress of the deposit sediment decreased (Equation 5). The mobilization of debris flow was enhanced when entering the lateral flume.

As shown in Figs. 15 and 16, the lobe height increased with released flow

volume for all of the tests whilst the ratio of lobe height to lobe length was slightly affected by the released flow volume. The entrainment volume increased with released volume (Fig. 6) and thus the lobe height increased. Compared with the flow volume, the grain composition of the debris flow after sediment entrainment had a more significant effect on the deposition process by affecting the basal shear stress and flow velocity.

As shown in Fig. 17, the lobe area increased with released flow volume for the FEC and FEW due to the increase of entrainment volume. The lobe area of the FEC ranged from 0.30–0.86 m^2 which was smaller than that of the FEW for the same released flow volume. The reason is that the ratio of lobe height to lobe length and slope angle of the FEC were larger than those of the FEW (Fig. 16). The lobe area of the FEC increased with flow-front density for 0.04 m^3 released flow but decreased with flow-front density for 0.07 m^3 released flow. This trend was not consistent with that of the FEW. The lobe area was affected by the entrainment volume, lobe height and ratio of lobe height to lobe length.

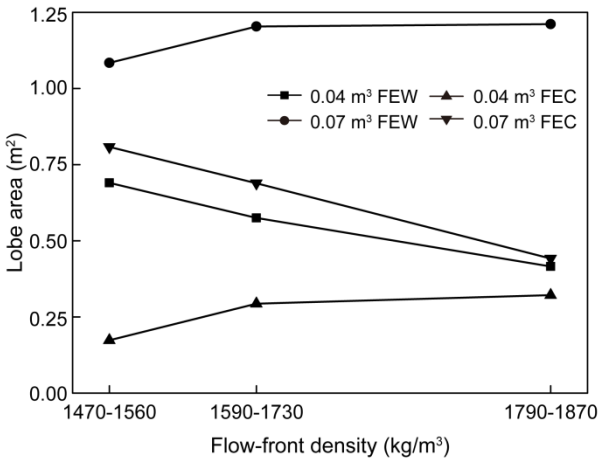

Fig. 17. Effects of flow volume and flow density on the lobe area.

5.2 Effect of water depth on deposit lobes

The variation of deposit morphology for the FEW was more pronounced than that of the FEC under the confinement of the water in the lateral flume. The lobe area of the FEW was reduced by more than 30% by comparing tests 6 and 7 and tests 13 and 14. Additionally, the lobe height increased by more than 17%. By contrast, the lobe area of the FEC decreased by about 25% by comparing tests 9 and 10, tests 16 and 17 and tests 20 and 21. Moreover, the lobe height increased by less than 12% for the FEC. The ratio of lobe height to lobe length increased by more than 60% for the FEW compared to less than 20% for the FEC. The reason is that the basal shear stress of the FEW was small (Equation 5), contributing to a larger lobe area and deposit length (Fig. 17). The flow motion in the lateral flume was significantly suppressed by the viscous drag imposed by the water. However, the basal shear stress of the FEC was relatively high and the effect of viscous drag of the water in the lateral flume on the flow movement was relatively limited. A simplified calculation was conducted to compare the drag stress p_d and basal shear stress R_s of the FEW and FEC,

$$b = \frac{R_s}{p_d} \tag{6}$$

$$p_d = C_d \rho_w U^2 \tag{7}$$

where ρ_w was the water density (1000 kg/m^3). C_d values were 0.08 and 0.4, respectively, for tests 7 and 10 based on the formula of drag coefficient proposed by Pudasaini (2012). b values were 0.33 and 2.05, respectively, for tests 7 and 10, indicating the drag stress for test 7 had a greater effect on the deposit process than for test 10.

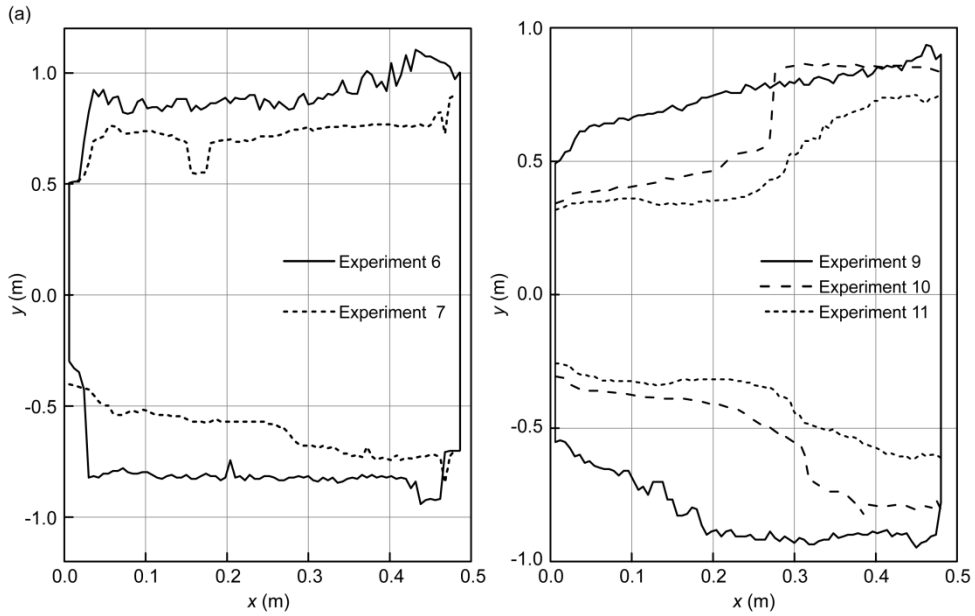

Fig. 18. Effect of water depth on the lobe area: (a) FEW (tests 6 and 7) and (b) FEC (tests 9, 10 and 11).

As shown in Fig. 18, the deposit length of the FEW was generally reduced uniformly in the direction perpendicular to the lateral flume, affected by the viscous drag stress. It was significantly reduced at the tributary flume exit for the FEC and slightly reduced at the opposite sidewall of the lateral flume with an increase of the water depth. The reason is that initially deposited sediment for the FEC was pushed aside by subsequent flow, while the latter flow was deposited directly at the tributary flume exit. Compared with deposit sediment at the tributary flume exit, the effect of viscous drag stress on the deposit sediment at the opposite sidewall of the lateral flume was reduced due to the thrust from the subsequent flows. An analysis was conducted to compare the thrust stress T_s of the FEW and FEC (Fig. S4),

$$d = \frac{T_{sw}}{T_{sc}} \tag{8}$$

$$T_s = p_s - R_s \tag{9}$$

where p_s is the sliding stress generated by gravity. d was 0.58 by comparing tests 7 and 10, indicating the thrust stress in test 10 had a much significant effect on the deposition process than in test 7.

6. Discussion

6.1 Blockage pattern

The blockage pattern of debris flows in the lateral flume can be classified as partial, submersed or complete. Two types of partial blockage occurred in our experiments. For the flows without sediment entrainment, the debris sediment concentrated at the opposite sidewall of the lateral flume and the slurry was deposited close to the tributary flume exit, manifesting the separation between the phases in the debris mixture. Such a phenomenon has been modelled and simulated by Pudasaini and Fischer (2020b). Due to a low flow velocity, the debris flow in test 8 was deposited at the tributary flume exit. The lateral flume was partially blocked by the debris flow in tests 1–4 and 8 which was ascribed to a relatively small sediment volume. Partial blockage was widely observed in the natural debris flows around Yingxue town, located near the epicenter of the Wenchuan earthquake (Tang et al., 2011a).

For tests 7, 11, 14, 17 and 21, submersed blockage occurred when the lobe width was equal to the lateral flume width and the water on both sides of the deposit lobe remained connected in the lateral flume. Submersed blockage occurred for the Namasha, Taoyuan and Liugui debris flows triggered by the Morakot typhoon. These flows had a mean flow depth of approximately 0.6 m, which was smaller than the

water depth of the river (Chen et al., 2019). For other flows after the entrainment of bed sediment, the lateral flume was completely blocked by the tributary debris flow and water in the lateral flume was separated into two parts by the lobe. The typical cases are the blockages of the Nanya River by debris flows in Hougou gully and Majingzi gully and of the Zhuma River by debris flow in the Xiongjia gully (Ni et al., 2014). The deposited volumes were large enough to enable complete blockage by the entrained sediment during the transportation process.

6.2 Comparison between debris-flow fans and deposit lobes

The deposit lobes of our experimental debris flows in the longitudinal section have morphological similarity with debris-flow fans unconstrained by sidewalls of the lateral flume conducted by Tsai (2006). The longitudinal profiles of deposit lobes and debris-flow fans can be described by Gaussian curves. The ratio of height to length of debris-flow fans ranges from 0.04–0.22 which is consistent with the experimental deposit lobes presented here. The ratios of lobe height to lobe length of debris-flow fans without mud are greater than the values with mud which is indicated by deposit lobes presented here.

There are morphology differences between deposit lobes and debris-flow fans in the transverse profiles. Constrained by the opposite sidewall of the lateral flume, the maximum deposit width is equal to the lateral flume width (0.5 m) in our experiments which is significantly smaller than the deposit length. By contrast, the maximum width measured in debris-flow fans has the same magnitude as the fan length (Tsai, 2006). The maximum deposit thickness occurs close to the opposite sidewall of the

lateral flume for our experimental lobes. Nevertheless, the maximum deposit thickness is located at the tributary flume exit for a debris-flow fan. The areas of deposit lobes on the horizontal plane form the shapes of dumbbells or trapezoids whilst they are circular for debris-flow fans. In addition, the deposits form coarse-grained lateral levees and frontal snout margins for debris flows without the sidewall of the lateral flume (de Haas et al., 2020; de Lange et al., 2020). By contrast, debris sediment was poorly sorted in our experiments due to the debris flows strongly mixing with the surges rebounding from the opposite sidewall or water in the lateral flume.

6.3 Flow regime

Dimensionless parameters estimated for natural debris flows and physical models are compared in order to evaluate quantitatively the similarity in flow regimes of experimental and natural debris flows (Stancanelli et al., 2015; Baselt et al., 2021). The following dimensional quantities have been considered to derive these dimensionless parameters: flow depth H, volume concentration C_v, grain density ρ_s, mean diameter d_s of the debris sediment, slurry density ρ_f, slurry viscosity μ_f and flow velocity U (Table S1). Since these flow parameters vary during debris flow motion (Pudasaini and Mergili, 2019), the dimensionless parameters for the flow front at the tributary flume exit are calculated.

Collisional, frictional, and viscous forces are considered to resist motion in debris flows (Iverson, 1997; Parsons et al., 2001; Iverson and Denlinger, 2001; de Haas et al., 2020; Baselt et al., 2021). Inertial forces result from short-term collisions

between sediment grains, frictional forces are related to continuous contacts between grains, and viscous forces are controlled by the slurry viscosity (Pudasaini and Mergili, 2019). Three dimensionless parameters describe the relative importance of these forces. The Savage number N_{Sav} describes the ratio of collisional to frictional forces,

$$N_{Sav} = \frac{\rho_s d_s^2 \gamma^2}{\left(\rho_s - \rho_f\right) gH \tan\varphi} \tag{10}$$

where φ is the angle of internal friction (Table 3).

The Bagnold number N_{Bag} defines the ratio of collisional to viscous forces,

$$N_{Bag} = \frac{C_v \rho_s \gamma d_s^2}{\left(1 - C_v\right) \mu_f} \tag{11}$$

where γ is the flow shear rate (1/s),

$$\gamma = \frac{U}{H} \tag{12}$$

The interstitial fluid viscosity μ_f was estimated as (Iverson, 1997)

$$\mu_f / \mu_w = 1 + 2.5C_{vf} + 10.05C_{vf}^2 + 0.00273\exp\left(16.6C_{vf}\right) \tag{13}$$

where μ_w is the dynamic viscosity of pure water (0.001 Pa s) and C_{vf} is the volume fraction of the interstitial fluid occupied by the fine component.

The friction number N_{Fri} defines the ratio of frictional to viscous forces,

$$N_{Fri} = \frac{C_v \left(\rho_s - \rho_f\right) gH \tan\varphi}{\left(1 - C_v\right) \gamma \mu_f} \tag{14}$$

The effects of particle collisions and slurry viscosity are indicated by the grain Reynolds number N_{Rg} (Iverson, 1997), which is defined as the ratio between the solid inertial stress and the fluid viscous shearing stress,

$$N_{Rg} = \frac{\rho_f \gamma d_s^2}{\mu_f} \tag{15}$$

Using the magnitudes of these dimensionless parameters to signify the transition between flow regimes was proposed by Iverson (1997). A debris flow tends to be dominated by grain collisions (inertial regime) when N_{Sav}>0.1 (Iverson and Denlinger, 2001). Collisional forces dominate over viscous forces for N_{Bag}>200, and frictional forces dominate over viscous forces for N_{Fri}>2000 (Bagnold, 1954; Savage and Hutter, 1989). By contrast, experimental data for water-saturated small-scale debris flows (Parsons et al., 2001) suggest that frictional forces began dominating viscous forces at N_{Fri}>250 for the flow front. Generally, debris flows with respect to grains begin to show inertial effects and deviate significantly from ideal viscous behavior when N_{Rg}>1 (Vanoni, 1975).

As shown in Fig. 19(a), collisional forces were dominated by viscous forces for each experiment. N_{Bag} of the FEC and FEW were smaller than for flows without sediment entrainment. The flow depth increased and shear rate decreased after entrainment of the bed sediment (Table S1). Thus, the effect of collisional forces became less important relative to viscous forces. This trend was more obvious for the FEC than for the FEW. This is in contrast to experimental flows by Baselt et al. (2021) due to a low fluid viscosity and high shear rate. For flows without sediment entrainment, collisional forces dominated over frictional forces (Fig. 19(b)). By contrast, collisional forces were dominated by frictional forces for the flows after the entrainment of bed sediment. The relative influence of frictional forces increased by the entrainment of bed sediment due to a higher volumetric sediment concentration.

The effect of frictional forces in the FEC was more significant than in the FEW as a result of higher shear strength of coarse-grained bed sediment (Table 3). These findings strongly support the importance of the frictional and viscous forces in the multi-phase mechanical erosion model presented by Pudasaini and Fischer (2020a).

Observations from debris flow movement imply that frictional forces dominated over viscous forces for each test. This suggests that the boundaries proposed by Bagnold (1954) and Savage and Hutter (1989) based on dry flow experiments are not applicable to our experimental debris flows. As shown in Fig. 19(c), this transition coincides with the regime boundary suggested by Parsons et al. (2001) based on debris-flow experiments. As shown in Fig. 19(d), grain inertia always plays a more important role than the fluid inertia because of the interactions of dense debris grains. FEW have a much more significant grain inertia than FEC due to a higher flow velocity. These dimensionless parameters highlight the importance of the material properties and bed sediment entrainment in determining the developed flow regime (Pudasaini and Mergili, (2019); Pudasaini and Fischer (2020a)).

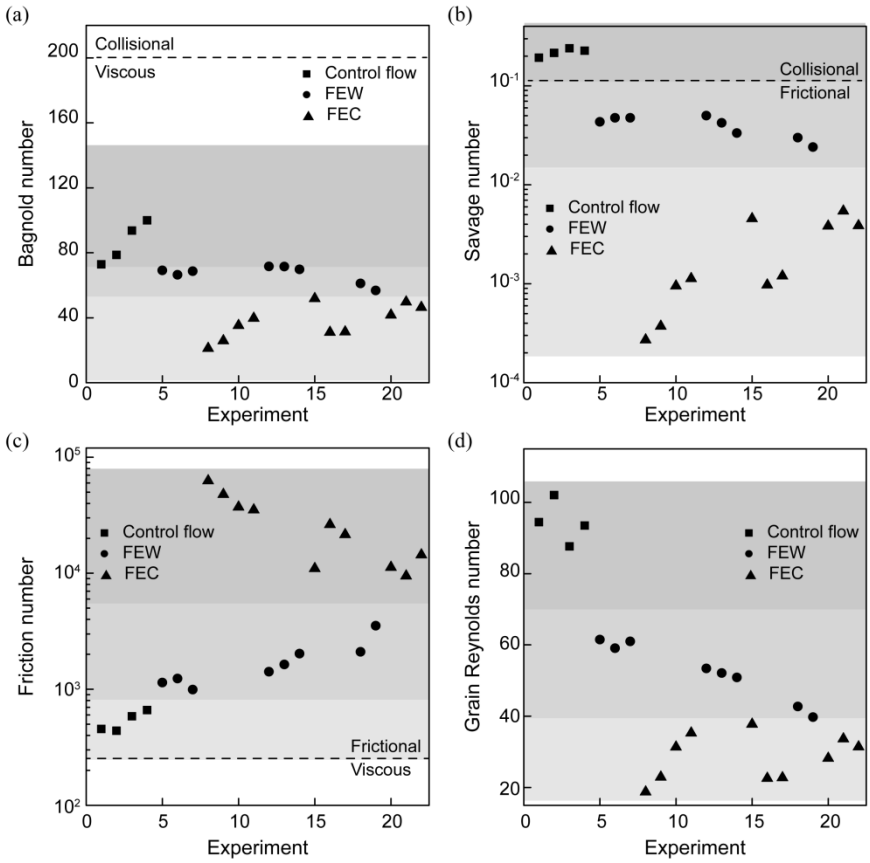

Fig. 19. Effects of bed sediment on the flow regime: (a) Bagnold number; (b) Savage number; (c) friction number; (d) grain Reynolds number.

6.4 Scaling issues

As shown in Table 4, the dimensionless numbers representing flow dynamics of our experimental debris flows vary within the ranges of values that developed in the large-scale USGS flume and in natural debris flows (Iverson, 1997; Iverson and Denlinger, 2001; Zhou and Ng, 2010). Nevertheless, the width of the tributary flume in our experiments is less than twice that of the lateral flume. This situation is suitable for the deposit process of debris flow in a tributary stream. The water in the lateral flume is static and it is suitable for streams with Froude number $F_{rm} < 1$ (Pudasaini, 2014).

Table 4. Physical and dimensionless parameters estimated for the present laboratory experiments and large-scale, natural debris flows

Parameter	Symbol (Unit)	Present tests	USGS Flume Debris Flows [a]	Natural Debris Flows [a, b, c]
Typical grain diameter	d_s (m)	0.001–0.002	0.001	10^{-5}–10
Flow depth	H (m)	0.02–0.07	0.1	0.1–10
Flow shear rate	γ (1/s)	5–105	100	1–100
Solid density	ρ_s (kg/m^3)	2700	2700	2500–3000
Fluid density	ρ_f (kg/m^3)	1000–1207	1100	1000–1200
Solid volume fraction	C_v (–)	0.3–0.5	0.6	0.4–0.8
Fluid viscosity	μ_f (Pa s)	0.001–0.0015	0.001	0.001–0.1
Friction angle	ϕ (deg)	27–33	40	25–45
Savage number	N_{Sav}	0.001–0.24	0.2	10^{-7}–10^{0}
Bagnold number	N_{Bag}	21–100	400	10^{0}–10^{8}
Friction number	N_{Fri}	365–77914	2000	10^{0}–10^{5}
Grain Reynolds number	N_{Rg}	19–106	100	0.01–2

[a]Iverson (1997).

[b]Iverson and Denlinger (2001).

[c]Zhou and Ng (2010).

Deposit morphology and blockage pattern of our small-scale experimental debris flows are similar to those of natural debris flows deposited in a tributary stream. The swollen and flat lobes, implying that the deposit morphology of debris flows is

strongly affected by the entrainment of bed sediment, are present in natural debris flows observed in the Kamikamihorizawa Creek (Okano et al., 2012). The partial, submersed and complete blockages observed in the experimental debris flows are inferred for natural debris flows at channel confluences (Tang et al., 2011a; Tang et al., 2011b; Ni et al., 2014; Chen et al., 2019).

7. Conclusions

We experimentally investigated the effects of bed-sediment entrainment and water depth in the lateral flume on the deposition characteristics of debris flows. The experimental results are suitable for the deposition process of debris flow in a tributary stream with Froude number $F_{rm} < 1$. The main conclusions are listed as follows:

(1) The shapes of deposit lobes displayed significant differences, affected by the entrained sediment. The deposit lobes of flows without sediment entrainment were a typical alluvial fan compressed by the opposite sidewall of the lateral flume. For flows after the entrainment of widely graded (FEW) and coarse-grained bed sediments (FEC), the depositions were shaped as flat and swollen lobes, respectively. The lobe area of debris flows on the horizontal plane formed the shapes of dumbbells or trapezoids, depending on the sediment volume. The cross sections of the lobes along the lateral flume presented a Gaussian distribution for flows after the entrainment of bed sediments.

(2) The lobe height increased with released flow volume for all of the tests. The ratio of lobe height to lobe length increased after bed-sediment entrainment. The

increased magnitude of FEW was lower than that of FEC with the same released volume. This was due to a higher basal shear resistance and a smaller flow velocity. The ratio of lobe height to lobe length decreased with the increase of the flow density as a result of the viscous slurry.

(3) The lobe area decreased and lobe height increased with increasing water depth due to the drag stress of the water in the lateral flume. The water depth in the lateral flume had a more significant influence on the lobes of the FEW than those of the FEC. The deposit length was generally reduced uniformly in the direction perpendicular to the lateral flume for the FEW, while the deposit length was significantly reduced at the tributary flume exit and slightly reduced near the opposite sidewall of the lateral flume for the FEC.

(4) The blockage patterns of debris flows can be partial, submersed or complete, depending on the flow volume and water depth in the lateral flume. The debris sediment was poorly sorted in the depth direction of the lobe. However, a bedding structure of the gravel was developed at the surface of the lobe.

These results suggest that bed-sediment entrainment upstream and water depth have a significant influence on the debris-flow behavior and blockage patterns. Debris-flow runout and inundation models should include the effect of bed sediment on the debris flow to accurately describe the deposition of the flow. Further research will focus on the deposition process of debris flow in a lateral flume with different slopes and flow velocities.

Acknowledgements

The authors are grateful to the editor and two anonymous reviewers for their precious review comments and constructive suggestions. We acknowledge funding from the Natural Science Foundation of China (grant Nos. 42007252, 41731283 and 41877234).

References

Bagnold, R.A., 1954. Experiments on a gravity-free dispersion of large solid spheres in a Newtonian fluid under shear. Proc. R. Soc. A, 225 (1160), 49–63. https://doi.org/10.1098/rspa.1954.0186.

Baselt, I., Oliveira, G., Fischer, J.T., Pudasaini, S.P., 2021. Evolution of stony debris flows in laboratory experiments. Geomorphology, 372, 107431.

Berger, C., McArdell, B.W., Fritschi, B., Schlunegger, F., 2010. A novel method for measuring the timing of bed erosion during debris flows and floods. Water Res. 46, W02502.

Blair, T.C., McPherson, J.G., 1998. Recent debris-flow processes and resultant form and facies of the dolomite alluvial fan, Owens Valley, California. J. Sediment. Res. 68, 800–818.

Bollschweiler, M., Stoffel, M., Ehmisch, M., Monbaron, M., 2007. Reconstructing spatiotemporal patterns of debris-flow activity using dendrogeomorphological methods. Geomorphology, 87 (4), 337–351.

Bryant, M., Falk, P., Paola, C., 1995. Experimental study of avulsion frequency and rate of deposition. Geology, 23 (4), 365–368.

Chen, K.T., Chen, X.Q., Hu, G.S., Kuo, Y.S., Huang, Y.R., Shieh, C.L., 2019. Dimensionless assessment method of landslide dam formation caused by tributary debris flow events. Geofluids, 2019, 1–14.

Clarke, L., Quine, T.A., Nicholas, A., 2010. An experimental investigation of autogenic behaviour during alluvial fan evolution. Geomorphology, 115 (3), 278–285.

Coussot, P., Laigle, D., Arattano, M., Deganutti, A., Marchi, L., 1998. Direct determination of rheological characteristics of debris flow. J. Hydraul. Eng. 124 (8), 865–868.

D'Agostino, V., Cesca, M., Marchi, L., 2010. Field and laboratory investigations of runout distances of debris flows in the Dolomites (Eastern Italian Alps). Geomorphology, 115 (3), 294–304.

Dang, C., Cui, P., Cheng, Z.L., 2009. The formation and failure of debris flow-dams, background, key factors and model tests: case studies from China. Environ. Geol. 57, 1901–1910.

de Haas, T., Berg, W., Braat, L., Kleinhans, M.G., 2016. Autogenic avulsion, channelization and backfilling dynamics of debris-flow fans. Sedimentology, 63, 1596–1619.

de Haas, T., Densmore, A.L., Stoffel, M., Suwa, H., Imaizumi, F., Ballesteros-Cánovas, J.A., Wasklewicz, T., 2017. Avulsions and the spatio-temporal evolution of debris-flow fans. Earth-Sci. Rev. 177, 53–75.

de Haas, T., Santa, N., de Lange, S.I., Pudasaini, S.P., 2020. Similarities and contrasts between the subaerial and subaqueous deposits of subaerially triggered debris flows: An analogue experimental study. J. Sediment. Res. 90(9), 1128–1138.

de Haas, T., van Woerkom, T., 2016. Bed scour by debris flows: experimental investigation of effects of debris-flow composition. Earth Surf. Proc. Landf. 41, 1951–1966.

de Lange, S.I., Santa, N., Pudasaini, S.P., Kleinhans, M.G., de Haas, T., 2020. Debris-flow generated tsunamis and their dependence on debris-flow dynamics. Coast. Eng. 157, 103623.

Domnik, B., Pudasaini, S.P., 2012. Full two-dimensional rapid chute flows of simple viscoplastic granular materials with a pressure-dependent dynamic slip-velocity and their numerical simulations. J. Non-Newton. Fluid Mech. 173–174, 72–86.

Dong, J. J., Li, Y.S., Kuo, C.Y., Sung, R.T., Li, M.H., Lee, C.T., Chen, C.C., Lee, W.R., 2011. The formation and breach of a short-lived landslide dam at Hsiaolin village, Taiwan—part I:

post-event reconstruction of dam geometry. Eng. Geol. 123 (1-2), 40–59.

Dowling, C.A., Santi, P.M., 2014. Debris flows and their toll on human life: a global analysis of debris-flow fatalities from 1950 to 2011. Nat. Hazards 71, 203–227.

Godt, J.W., Coe, J.A., 2007. Alpine debris flows triggered by a 28 July 1999 thunderstorm in the central Front Range, Colorado. Geomorphology, 84, 80–97.

Hürlimann, M., McArdell, B.W., Rickli, C., 2015. Field and laboratory analysis of the runout characteristics of hillslope debris flows in Switzerland. Geomorphology, 232, 20–32.

Iverson, R. M., 1997. The physics of debris flows. Rev. Geophys. 35 (3), 245–296.

Iverson, R. M., Denlinger, R.P., 2001. Flow of variably fluidized granular masses across three-dimensional terrain: 1. Coulomb mixture theory. J. Geophys. Res. 106 (B1), 537–552.

Jakob, M., Friele, P., 2010. Frequency and magnitude of debris flows on Cheekye River, British Columbia, Geomorphology 114 (3), 382–395.

Kafle, J., Kattel, P., Mergili, M., Fischer, J.T., Pudasaini, S.P., 2019. Dynamic response of submarine obstacles to two-phase landslide and tsunami impact on reservoirs. Acta Mech. 230, 3143–3169.

Liu, J., You, Y., Chen, X., Liu, J., Chen, X., 2014. Characteristics and hazard prediction of large-scale debris flow of Xiaojia Gully in Yingxiu Town, Sichuan Province, China. Eng. Geol. 180, 55–67.

Liu, T., Li. C., Fan, B., 2012. Experimental study on flow pattern and sediment transportation at a 90 open-channel confluence. Int. J. Sediment Res. 27 (2), 178–187.

Major, J.J., Iverson, R.M., 1999. Debris-flow deposition: Effects of pore-fluid pressure and friction concentrated at flow margins. Geol. Soc. Am. Bull. 111 (10), 1424–1434.

Major, J.J., Pierson, T.C., 1992. Debris flow rheology: Experimental analysis of fine-grained slurries. Water Resour. Res. 28 (3), 841–857.

Major, J.J., 1995. Experimental studies of deposition at a debris-flow flume, Reston, VA, USA: US Geological Survey. https://doi.org/10.3133/fs02894.

Mergili, M., Fischer, J.T., Krenn, J., Pudasaini, S.P., 2017. r. avaflow v1, an advanced open-source computational framework for the propagation and interaction of two-phase mass flows. Geosci. Model Dev. 10, 553–569. https://doi.org/10.5194/gmd-10-553-2017.

Mergili, M., Pudasaini, S.P., Emmer, A., Fischer, J.T., Cochachin, A., Frey, H., 2020. Reconstruction of the 1941 GLOF process chain at Lake Palcacocha (Cordillera Blanca, Peru). Hydrol. Earth Syst. Sci. 24(1), 93–114.

Ni, H., Zheng, W., Song, Z., Xu, W., 2014. Catastrophic debris flows triggered by a 4 July 2013 rainfall in Shimian, SW China: formation mechanism, disaster characteristics and the lessons learned. Landslides 11(5), 909–921.

Okano, K., Suwa, H., Kanno, T., 2012. Characterization of debris flows by rainstorm condition at a torrent on the Mount Yakedake volcano, Japan. Geomorphology, 136 (1), 88–94.

Parsons, J.D., Whipple, K.X., Simoni, A., 2001. Experimental study of the grain-flow, fluid-mud transition in debris flows. Geology, 109 (4), 427–447.

Peng, M., Ma, C.Y., Chen, H.X., Zhang, P., Zhang L.M., Jiang, M.Z., Zhang, Q.Z., Shi Z.M., 2021. Experimental study on breaching mechanisms of landslide dams composed of different materials under surge waves. Eng. Geol. 291, 106242.

Peng, M., Zhang, L.M., 2012. Breaching parameters of landslide dams. Landslides, 9 (1), 13–31.

Peng, M., Zhang, L.M., 2013. Dynamic decision making for dam-break emergency management -

part 2: Application to Tangjiashan Landslide Dam failure. Nat. Hazards Earth Syst. Sci. 13(2), 439–454.

Pudasaini, S.P., 2012. A general two-phase debris flow model. J. Geophys. Res.-Solid Earth 117, F03010.

Pudasaini, S.P., 2014. Dynamics of submarine debris flow and tsunami. Acta Mech. 225(8), 2423–2434.

Pudasaini, S. P., Mergili, M., 2019. A multi-phase mass flow model. J. Geophys. Res.-Earth Surf. 124, 2920–2942.

Pudasaini, S.P., Fischer, J.T., 2020a. A mechanical erosion model for two-phase mass flows. Int. J. Multiph. Flow 132, 103416.

Pudasaini, S.P., Fischer, J.T., 2020b. A mechanical model for phase separation in debris flow. Int. J. Multiph. Flow 129, 103292.

Savage, S.B., Hutter, K., 1989. The motion of a finite mass of granular material down a rough incline. J. Fluid Mech. 199, 177–215.

Shen, D.Y., Shi, Z.M., Peng, M., Zhang, L.M., Jiang, M.Z., 2020. Longevity analysis of landslide dams. Landslides, 17(8), 1797–1821.

Shi, Z., Zheng, H., Yu, S., Peng, M., Jiang, T., 2018. Application of CFD-DEM to investigate seepage characteristics of landslide dam materials. Comput. Geotech. 101, 23–33.

Shugar, D.H., Jacquemart, M., Shean, D., Bhushan, S., Upadhyay, K., Sattar, A., et al., 2021. A massive rock and ice avalanche caused the 2021 disaster at Chamoli, Indian Himalaya. Science 373 (6552), 300–306.

Stancanelli, L.M., Lanzoni, S., Foti, E., 2015. Propagation and deposition of stony debris flows at

channel confluences. Water Resour. Res. 51 (7), 5100–5116.

Stoffel, M., Mendlik, T., Schneuwly-Bollschweiler, M., Gobiet, A., 2014. Possible impacts of climate change on debris-flow activity in the Swiss Alps. Clim. Change, 122(1–2), 141–155.

Suwa, H., 2017. Pulsation in debris flows and its mechanism, International Journal of Erosion Control Engineering, 10(1), 16–23.

Tang, C., Zhu, J., Ding, J., Cui, X., Chen, L., and Zhang, J., 2011a. Catastrophic debris flows triggered by a 14 August 2010 rainfall at the epicenter of the Wenchuan earthquake. Landslides 8(4), 485–497.

Tang, C., Rengers, N., Van Asch, T.W.J., Yang, Y.H., Wang, G.F., 2011b. Triggering conditions and depositional characteristics of a disastrous debris flow event in Zhouqu city, Gansu Province, northwestern China. Nat. Hazards Earth Syst. Sci. 11, 2903–2912.

Tsai, Y.F., 2006. Three-dimensional topography of debris-flow fan. J. Hydraul. Eng. 132(3), 307–318.

Vanoni, V. A., 1975. Sedimentation Engineering, Am. Soc. of Civil Eng., New York.

Wang, G., Sassa, K., Fukuoka, H., 2003. Downslope volume enlargement of a debris slide–debris flow in the 1999 Hiroshima, Japan, rainstorm. Eng. Geol. 69, 309–330.

Zheng, H., Shi, Z., Peng, M., Yu, S., 2018. Coupled CFD-DEM model for the direct numerical simulation of sediment bed erosion by viscous shear flow. Eng. Geol. 245, 309–321.

Zheng, H., Shi, Z., Shen, D., Peng, M., Hanley, K.J., Ma, C., Zhang, L., 2021. Recent advances in stability and failure mechanisms of landslide dams. Front. Earth Sci. 9:659935.

Zhou, G.G., Ng, C.W., 2010. Dimensional analysis of natural debris flows. Can. Geotech. J. 47 (7), 719–729.

Supplementary Information for "Deposition characteristics of debris flows in a lateral flume considering upstream entrainment"

Contents:

Considering the large displacement and deformation of bed sediment in the processes of erosion and deposition, we conducted ring shear tests (GCTS, SRS-150) to obtain the shear strengths under drainage conditions. The normal stresses were 25 kPa, 50 kPa, 75 kPa and 100 kPa, as shown in Fig. S1. The shear rate was 1°/min and the shear angle was 30°.

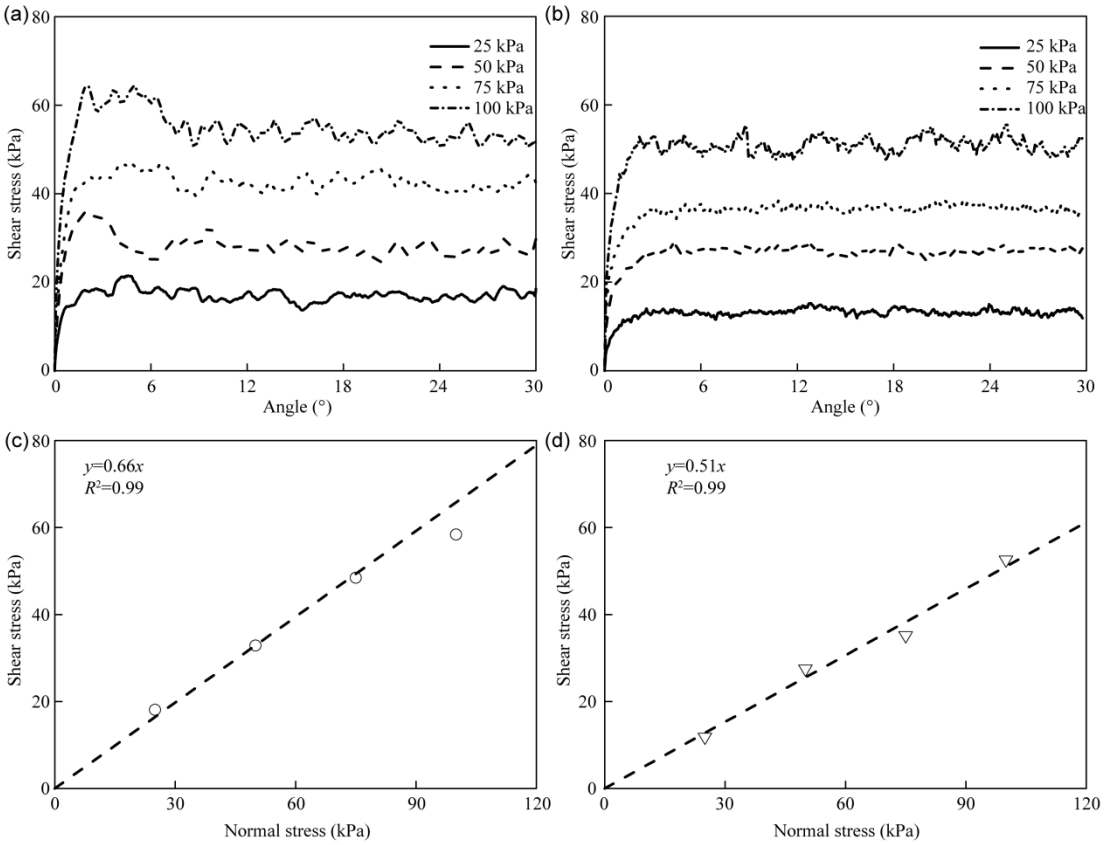

Figure. S1. Curves of shear stress and shear strain: (a) coarse-grained bed sediment; (b) widely graded bed sediment. Curves of peak shear stress and normal stress: (c) coarse-grained bed sediment; (d) widely graded bed sediment.

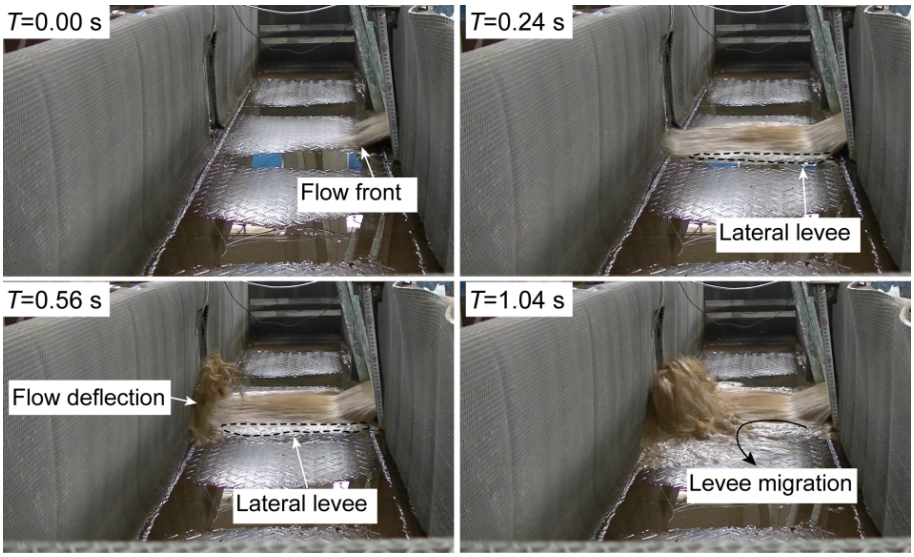

Fig. S2. Deposition process of debris flow in the lateral flume without a water stream in test 5. Debris flow was just entering the lateral flume at T=0.00 s.

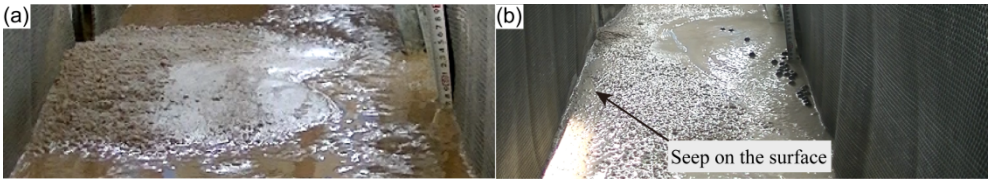

Fig. S3. Comparison of the deposit lobes in tests 6 (a) and 19 (b). Seeps and small springs developed on lobe surfaces formed by flows with released flow densities of 1700 kg/m^3. No water escaped the lobes formed by released flows with densities 1000 kg/m^3.

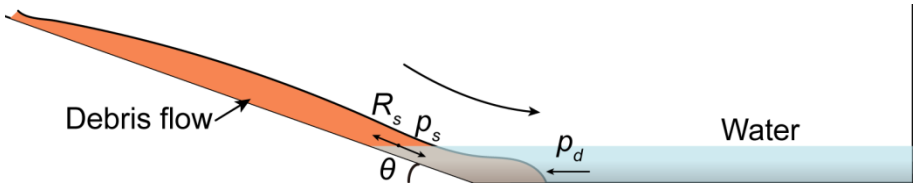

Fig. S4. Comparison of the thrust stress T_s of the flows after the entrainment of widely graded and coarse-grained bed sediments. $T_s = p_s$-R_s, where p_s is the sliding stress generated by gravity ($\rho g H \sin\theta$), R_s is the basal shear stress and p_d is the viscous drag stress. The excess pore pressure is not considered.

Table S1. Dimensionless parameters estimated for experimental debris flows

Case	ρ_s (kg/m^3)	ρ_f (kg/m^3)	U (m/s)	H (m)	γ (/s)	C_{vf}	μ_f (Pa s)	tan(φ)	C_v	d_s (m)	N_B	N_S	N_F	N_{RG}	F_{rd}
1	2700	1127	2.00	0.0192	104.17	0.07	0.0012	0.514	0.237	0.001	72.8	0.192	378.4	97.8	4.73
2	2700	1127	2.25	0.02	112.50	0.07	0.0012	0.514	0.237	0.001	78.6	0.215	365.0	105.7	5.21
3	2700	1207	1.75	0.0166	105.42	0.12	0.0015	0.514	0.330	0.001	93.6	0.240	390.1	84.8	4.45
4	2700	1207	2.25	0.02	112.50	0.12	0.0015	0.514	0.330	0.001	99.9	0.227	440.4	90.5	5.21
5	2700	1000	1.50	0.0244	61.48	0.00	0.0010	0.514	0.294	0.001	69.2	0.049	1417.6	61.5	3.14
6	2700	1000	1.50	0.0254	59.06	0.00	0.0010	0.514	0.294	0.001	66.4	0.043	1536.2	59.1	3.08
7	2700	1000	1.50	0.0246	60.98	0.00	0.0010	0.514	0.294	0.001	68.6	0.048	1440.9	61.0	3.13
8	2700	1000	0.38	0.08	4.69	0.00	0.0010	0.657	0.294	0.002	21.1	0.000	77914.9	18.8	0.43
9	2700	1000	0.50	0.0872	5.73	0.00	0.0010	0.657	0.294	0.002	25.8	0.000	69428.1	22.9	0.55
10	2700	1000	0.50	0.0638	7.84	0.00	0.0010	0.657	0.294	0.002	35.3	0.001	37165.8	31.3	0.65
11	2700	1000	0.60	0.068	8.82	0.00	0.0010	0.657	0.294	0.002	39.7	0.001	35183.5	35.3	0.75
12	2700	1127	1.25	0.022	56.82	0.07	0.0012	0.514	0.364	0.001	73.2	0.050	1465.7	53.4	2.76
13	2700	1127	1.38	0.0248	55.44	0.07	0.0012	0.514	0.364	0.001	71.5	0.042	1693.2	52.1	2.86
14	2700	1127	1.63	0.03	54.17	0.07	0.0012	0.514	0.364	0.001	69.8	0.033	2096.5	50.9	3.07
15	2700	1127	0.75	0.042	17.86	0.07	0.0012	0.657	0.364	0.0015	51.8	0.005	11379.9	37.7	1.20
16	2700	1127	0.75	0.0702	10.68	0.07	0.0012	0.657	0.364	0.0015	31.0	0.001	31791.9	22.6	0.93
17	2700	1127	0.63	0.058	10.78	0.07	0.0012	0.657	0.364	0.0015	31.2	0.001	26042.3	22.8	0.85
18	2700	1207	1.63	0.0316	51.42	0.12	0.0015	0.514	0.397	0.001	61.0	0.030	2034.4	41.4	2.99
19	2700	1207	1.63	0.034	47.79	0.12	0.0015	0.514	0.397	0.001	56.7	0.024	2355.1	38.4	2.89
20	2700	1207	0.63	0.0401	15.59	0.12	0.0015	0.657	0.397	0.0015	41.6	0.004	10887.2	28.2	1.02
21	2700	1207	0.75	0.0403	18.61	0.12	0.0015	0.657	0.397	0.0015	49.7	0.005	9163.4	33.7	1.22
22	2700	1207	0.85	0.049	17.35	0.12	0.0015	0.657	0.397	0.0015	46.3	0.004	11953.1	31.4	1.26